PCCP

PAPER

View Article Online
View Journal | View Issue

Cite this: *Phys. Chem. Chem. Phys.*, 2014, **16**, 13875

Photo-physical properties of 2-(1-ethynylpyrene)-adenosine: influence of hydrogen bonding on excited state properties†

P. Trojanowski,[a] J. Plötner,[a] C. Grünewald,[b] F. F. Graupner,[c] C. Slavov,[a] A. J. Reuss,[a] M. Braun,[a] J. W. Engels[b] and J. Wachtveitl*[a]

Received 17th March 2014,
Accepted 14th May 2014

DOI: 10.1039/c4cp01148a

www.rsc.org/pccp

The photo-physical properties of 2-(1-ethynylpyrene)-adenosine (PyA), a fluorescent probe for RNA dynamics, were examined by solvation studies. The excited-state dynamics display the influence of the vicinity on the spectral features. Combining improved transient absorption and streak camera measurements along with a new analysis method provide a detailed molecular picture of the photophysics. After intramolecular vibrational energy redistribution (IVR), two distinct states are observed. Solvent class (protic/aprotic) and permittivity strongly affect the properties of these states and their population ratio. As a result their emission spectrum is altered, while the fluorescence quantum yield and the overall lifetime remain nearly unchanged. Consequently, the hitherto existing model of the photophysics is herein refined and extended. The findings can serve as basis for improving the information content of measurements with PyA as a label in RNA.

Introduction

Monitoring dynamics of proteins, membranes or DNA/RNA depends on specific and versatile probes. Molecular fluorescence can be very sensitive depending on the molecule and its surroundings covering a great variety of lifetimes or spectral characteristics.[1] Therefore fluorophores are perfectly suited and thus ubiquitously applied as molecular probes. Pyrene is used often among the large number of fluorophores. The basic spectral characteristics and photo-dynamics of the monomer[2–8] as well as its excimer characteristics[2,9,10] are well studied. Numerous derivatives of pyrene were synthesized to examine the influence of substitutions,[8,11] artificial donor–acceptor systems,[12–15] its aggregation behaviour and ISC/IC dynamics.[16,17] A number of groups introduced pyrene into DNA to investigate electron transfer into nucleobases *via* photo-excitation of pyrene,[15,18–24] specific base/structure recognition,[25–30] FRET-pair studies,[30–32] molecular beacons,[33–35] hybridization probes[36–42] *etc.* and accomplished a remarkable understanding of the photo-physics and dynamics of pyrene coupled to deoxyribonucleic acid nucleosides. A great variety of fluorophores as probes for RNA were also synthesized, aiming for a structural and functional probe with minimal structural perturbation and optimal photo-physical properties,[43] which is challenging due to the greater structural flexibility and complexity of RNA.[44–47] Pyrene as a label has a small share of this variety in RNA. It was introduced with different linkers at different positions to the RNA nucleosides. One favoured position is the C2′ of ribose to detect ribonucleic acid[48–53] as well as to monitor hybridization[42,53,54] and folding.[55] C2′ was chosen because the label should point out of a typical A-helix structure motif. Another approach is the direct modification of the nucleobase and was applied to DNA nucleosides by groups like Wagenknecht,[15,18–24,36,39] Netzel,[56,57] Kim[37] and Berlin.[58]

We previously presented the 2-(1-ethynylpyrene)-adenosine (PyA, Fig. 1), a pyrene modified RNA nucleoside, where pyrene is attached at the 2-position of adenine.[59] This position was chosen in order to locate the pyrene in the minor groove of a RNA A-helix.

The photo-physics of a protected nucleoside form[60] as well as the applicability and the characteristics of PyA in modified 15-mer oligonucleotides[61] as a RNA folding probe were investigated.[62] Based on spectroscopic characteristics of CT states[12,63] and findings of other groups, which observed ICT states in similar systems[24,64] the proposed model of the photophysics involved an intramolecular charge transfer process (ICT).[61] This intramolecular charge transfer was suggested to take place from the pyrene to the adenine[64] and to be followed by a proton transfer to adenine.[60]

[a] *Institute for Physical and Theoretical Chemistry, Goethe University Frankfurt, Max-von-Laue-Straße 7, 60438 Frankfurt/Main, Germany. E-mail: wveitl@theochem.uni-frankfurt.de; Fax: +496979829709; Tel: +496979829351*

[b] *Institute for Organic Chemistry and Chemical Biology, Goethe University Frankfurt, Max-von-Laue-Straße 7, 60438 Frankfurt/Main, Germany*

[c] *Faculty of Physics, Center for Integrative Protein Science, Ludwig Maximilians University Munich, Oettingenstrasse 67, 80538 Munich, Germany*

† Electronic supplementary information (ESI) available: Em. spectra of PyA at 376 nm and 421 nm (Fig. S1), exc. spectra in MeOH and DMSO (Fig. S2), TA spectra of PyA in all solvents (Fig. S3) and comparison of experimental absorption spectra of PyA in DMSO with QC calculations (Fig. S4). See DOI: 10.1039/c4cp01148a

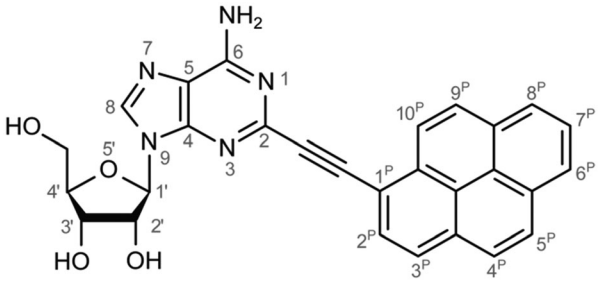

Fig. 1 Lewis structure of the pyrene modified adenosine 2-(1-ethynylpyrene)-adenosine (PyA).

However, it remained unclear whether a proton transfer indeed takes place and how the surrounding contributes to the spectral properties and dynamics of 2-(1-ethynylpyrene)-adenosine.

This study reports on the solvent dependence of the photo-induced dynamics by using steady-state, transient absorption and streak camera measurements as well as quantum chemical calculations and leads to a more complete picture of the photo-induced processes of 2-(1-ethynylpyrene)-adenosine.

Material and methods

Sample preparation

2-(1-Ethynylpyrene)-adenosine (PyA) was synthesized using methodologies described earlier for the synthesis of protected PyA.[59]

In summary, a solvent mixture of 60 ml of dimethylformamide and 5 ml of triethylamine was degassed thoroughly to exclude oxygen in the reaction mixture. 1.00 g (2.55 mmol, 1.00 eq.) of 2-iodoadenosine, 0.751 g (3.32 mmol, 1.30 eq.) of 1-ethynylpyrene, 84 mg (0.44 mmol, 17 mol%) of copper(I)iodide and 176 mg of bis(triphenylphosphine)palladium(II)chloride (0.25 mmol, 10 mol%) were added to the solvent mixture. The orange reaction mixture was stirred under argon for 19 h at room temperature. The mixture was filtered off to remove copper(I)iodide, the solution was adsorbed on silica gel and purified by column chromatography. Elution with a solvent mix of dichloromethane and methanol (9 : 1) and subsequent crystallization from methanol afforded 2-(1-ethynylpyrene)-adenosine as yellow powder in 80% yield.

A DMSO stock solution was diluted to prepare the samples in other solvents and therefore a remaining amount of 1%-DMSO is present in all solvents. As a side effect *t*BuOH remains liquid at room temperature ($\sim$23 °C).

Steady-state spectroscopy

Absorption spectra were recorded on a JASCO V670 absorption spectrometer between 300 nm and 600 nm using a fused silica cuvette with 1 mm optical path length. All spectra were background corrected for solvent absorption. In acetone, the spectrum was limited to 340 nm due to strong solvent absorption. The concentration of PyA for all absorption measurements varied between 150–200 μM.

Fluorescence spectra were taken on a JASCO FP-8500 fluorimeter between 360 nm and 700 nm using a fused silica cuvette with the dimensions 3 × 3 × 3 mm^3. The excitation wavelength varied between 371 nm and 376 nm depending on the exact position of the absorption maximum. The concentration was adjusted to approximately 0.1 OD/3 mm ($\sim$10 μM) to minimize reabsorption effects. The spectra were corrected for remaining reabsorption and the spectral properties of the detection system. Fluorescence quantum yields (Φ_{fl}) were obtained by a relative method with quinine bisulfate (10 μM, Φ_{fl} = 0.60 ± 0.02 at 350 nm in 0.5 M H_2SO_4 (ref. 65 and 66)). A cross reference with quinine bisulfate (10 μM) in 0.05 M H_2SO_4 at 366 nm was done to account for excitation wavelength and H_2SO_4 concentration specific variations.

Vis-pump–probe spectroscopy

The time resolved transient absorption (TA) measurements were performed using a self-built pump–probe setup.[67] Ultra short laser pulses (150 fs) were provided by a laser–amplifier system (Clark, MXR-CPA-2001) operating at a repetition rate of 1 kHz at a central wavelength of 775 nm. For the probe pulses, a single filament white light (WL) was generated by focusing the laser fundamental in a CaF_2 crystal of 5 mm thickness. The WL covered a spectral range between 350 nm and 700 nm and was focused to a diameter of $\sim$100 μm at the sample position. The pump pulses at 388 nm were produced by second harmonic generation (SHG) in a 0.1 mm BBO crystal (200 fs pulse duration) and focused to a diameter of $\sim$200 μm at the sample position. The pump pulse energy was adjusted to 100 nJ to avoid two-photon absorption processes (total amount of excited molecules $<$6%), even though no changes in dynamics were observed for pulse energies up to 250 nJ. Difference spectra of excited and unexcited samples were recorded by blocking every second laser pulse in the excitation pulse pathway using a chopper. Probe pulses were dispersed using a spectrometer resulting in a spectral resolution of 4 nm and recorded by a gated detection system. This detection system is composed of a 128 channel photodiode array (PDA) combined with a signal processing chip (Hamamatsu Photonics, S8865-128), a driver circuit (Hamamatsu Photonics, C9118) and a data acquisition card (National Instruments, NI-6120), which digitizes the analog PDA signals at 16 bits. The experiments were performed under magic angle conditions (54.7° pump–probe polarization angle difference) and continuous movement of the sample in the plane perpendicular to the direction of pulse propagation. The signal to noise ratio was 10^3 for an average of 6 scans (2.5 × 10^3 pulses per scan).

Streak camera spectroscopy

A Hamamatsu streak camera system (C5680-24 C) was employed to measure time-resolved fluorescence. For the femtosecond excitation pulses a CPA laser system (Clark, MXR-CPA-2001) at 780 nm was frequency doubled (390 nm) by second harmonic generation in a BBO crystal. The excitation energy varied between 40 nJ and 200 nJ depending on the sample and the time frame. It was focused onto the sample and detected under an angle of 15° to avoid excitation light to be collected. The excitation beam diameter was about 15 μm at the sample position. The induced fluorescence light was collected by an

air-gap achromat (f = 80 mm, 20 mm diameter, Type OUV 4.20, Bernhard Halle Nachfl. GmbH). The collimated fluorescence light passed a wire-grid polarizer (Moxtek UBB01C, diameter 36 mm) positioned at the magic angle before being focused with a second achromatic lens (f = 75 mm NUV, diameter 25 mm, Edmund Optics) onto the entrance slit of the spectrograph (Princeton Instruments, Acton Series SP2356, f = 300 mm, 50 lines per mm grating blazed at 600 nm). The slit widths were held to a minimum in order to achieve best temporal and spectral resolution. For further details of the setup see ref. 68. The spectrometer slit width was set between 5 μm and 15 μm corresponding to an overall wavelength resolution of 1.3 nm to 2 nm, respectively. The focal plane of the spectrograph coincided with the photocathode of the streak camera system. The time window was set by a fast single-sweep unit (Hamamatsu, M5677-01) with sweep velocities chosen accordingly to the investigated process. In the nanosecond regime, data were acquired in continuous sweeping mode. For detailed observation of the spectral shift in the picosecond regime time resolution was improved by deploying single sweeping combined with jitter correction using a fraction of excitation light as a temporal fix point in each frame. Therefore an overall time resolution of $<$5 ps, 6–20 ps, 40–50 ps and 80–100 ps was achieved for the corresponding time windows of 0.12 ns, 0.48 ns, 4.27 ns and 10.33 ns, respectively. For a more detailed explanation of the streak camera operation see ref. 69. All data were collected in photon-counting mode, typically yielding between 10^4 and 10^3 counts for one detection bin at the emission peak (bin defined by: wavelength width = spectral resolution, temporal width = effective width of instrumental response function). To collect sufficient fluorescence intensity for an adequate signal and reasonable statistics, excitation energy was chosen individually. However, in all experiments the photon flux was kept low enough to avoid pile-up artefacts. The total acquisition time for each measurement amounted to $\sim$15 min for the continuous streaking and $\sim$1 h for single sweep measurements. The sample solutions were pumped through a flow cell (fused silica, 0.5 mm light path length) to exchange the excited sample volume between consecutive laser pulses. All samples were prepared to yield less than 0.15 OD/mm absorbance required to match linear conditions avoiding reabsorption. The same sample preparation was used for all time frames. Therefore the total number of excitation shots accumulated for $\sim$2 ml of sample preparation with concentrations $\sim$70 μM typically amounted to 5×10^5. To prove intactness of the sample throughout the whole streaking experiment stationary absorption spectra were recorded using a spectrophotometer (LAMBDA 750, Perkin Elmer) and compared before and after the time resolved measurements.

Data analysis

Transient absorption. Transient absorption data were analysed first by conventional global lifetime analysis (GLA)[70] using a small number of discrete exponentials (typically $\leq$6). However, the high amount of spectrally and temporally interfering signals as well as the potential presence of non-exponential processes made the interpretation and the comparison of the resulting decay-associated spectra (DAS) very difficult. Thus, we do not present any of these results here. Instead, we have performed a lifetime density analysis (LDA), where the pre-exponential amplitudes in a sum of a large number ($>$50, typically $\sim$100) of exponential functions with fixed lifetimes are determined. Since the analysis is performed over the complete dataset it can be viewed as a more sophisticated extension of the GLA. In contrast to GLA, the LDA is model independent and naturally takes care of non-exponential or stretched exponential kinetics.[71]

The LDA was performed with the help of *OPTIMUS* – a newly developed time-resolved data analysis program in our group. The details about the program and the analysis methods used will be presented in detail elsewhere. Here we give only a short description of the LDA method to facilitate the discussion of the results.

The time-resolved data are quantitatively described by a spectrum of lifetimes, τ:

$$I(t) = \int_0^\infty \Phi(\tau) \mathrm{e}^{-t/\tau} \mathrm{d}\tau$$

where t is the time, $I(t)$ is the normalized decay function and $\Phi(\tau)$ is the spectral density function. In practice, the model is represented as a discrete sum of exponentials. In GLA the sum of less than 10 exponentials is used and thus $\Phi(\tau)$ becomes a spectrum (DAS) indicating roughly the maximum of each distribution, rather than a spectral density. In LDA, the used large set of exponentials is quasi-continuous and hence the spectral density function ($\Phi(\tau)$) can be obtained. Nevertheless, it is apparent that an inverse Laplace transform of $I(t)$ needs to be performed to recover the distribution ($\Phi(\tau)$) present in the transient. However, the inverse transform of the experimental dataset, which is inevitably incomplete and contains a certain amount of noise, is ill conditioned and will result in a highly ambiguous distribution ($\Phi(\tau)$) often with strongly oscillating values not justified by the experimental data. This problem is addressed by employing different regularization procedures to perform the numerical Laplace inversion. While in the typical least squares routines the sum of squared residuals is being minimized, the regularization introduces a second penalty term which improves the conditioning of the problem. Thus a function of the following form is iteratively minimized instead:

$$M = \sum_{j=1}^{n} \left(S_j - S_{\mathrm{fit},j}\right)^2 + \lambda^2 P^2$$

where S and S_{fit} are the experimental data and the fit, P is the penalty function which takes a specific form depending on the type of regularization used and λ is a Lagrange multiplier defining the relative importance of the two constraints.

Most commonly, in time-resolved spectroscopy (see ref. 72–77 and references therein) variants of the maximum entropy method[78] and Tikhonov regularization[79] are used. Currently OPTIMUS performs Tikhonov regularization and allows selection between several penalty functions. The search of the Lagrange multiplier can be performed either manually or with the help of dedicated search methods – the L-curve criterion,[80,81] the minimal product method[82,83] and generalized cross-validation.[75,84,85] The results

shown here were obtained using the identity matrix as a smoothing norm and an optimal value for the regularization parameter, determination based on the L-curve and generalized cross-validation methods.

The LDA recovers the lifetime distribution at each detection wavelength and thus the results can be presented in the form of a contour map, which, similarly to ref. 72, we call the lifetime density map (LDM). The reading of the maps is straightforward following the convention for DAS from GLA of transient absorption – positive pre-exponential amplitudes (red) describe either decay of absorption or the increase of bleaching/stimulated emission, while negative pre-exponential amplitudes (blue) reflect either decay of bleaching/stimulated emission or the increase of absorption. LDM allows easier comparison between different samples and different experimental conditions.

We should mention here that the de-convolution of the instrument response function and the fitting of the coherent oscillations at time zero caused by the interaction of the temporarily overlapping pump and probe beams are performed simultaneously using the numerical inverse Laplace transform. In *OPTIMUS*, the deconvolution of the IRF is implemented similarly to the procedure described in ref. 70, taking into account the wavelength dependent chirp. The coherent contributions at time zero are modelled as a sum of a Gaussian function and its first and second derivatives as in ref. 86.

Streak camera. The time-resolved fluorescence was analysed using a global Levenberg–Marquardt fitting procedure. By this nonlinear least-squares method the measured data were approximated with a linear combination of exponential decay functions convoluted with a Gaussian, accounting for the instrumental response function. The evaluation yields the time constants with corresponding decay associated spectra of the involved radiating processes (for a more detailed explanation of the general fitting procedure see ref. 87). Although the physical effect of a spectral shift might not be precisely represented as an exponential decay function, the phenomenon is sufficiently described by the approximation in the fluorescence analysis of this work to determine the time range and spectral characteristics. Due to the photon-counting method, noise or background signals are discriminated within the data acquisition process and do not have to be considered in the data processing.

Quantum-chemical calculations

All quantum-chemical calculations have been performed using the Turbomole[88] program package and the Q-Chem program.[89]

In this study, we use time-dependent density-functional theory (TDDFT)[90,91] and configuration-interaction singles methods (CIS)[92] (for an overview see *e.g.* ref. 93 and references therein). Both single reference methods are often used to study excited states of large molecules due to their relatively low computational cost.

TDDFT suffers from the electron-transfer self-interaction (SI) error, which results in an underestimation of the excitation energies of charge-transfer (CT) and Rydberg states.[94–99] The SI error is influenced by the amount of Hartree–Fock (HF) exchange in the used exchange correlation (xc) functional. This was pointed out by Dreuw *et al.*[94] To evaluate the influence of the SI error for the PyA system an exchange correlation (xc) functional study applying xc-functionals with different amounts of HF exchange has been performed (B-LYP: pure DFT functional, 0% HF exchange; B3-LYP: hybrid functional, 20% HF exchange; BH-LYP: hybrid functional, 50% HF exchange).

The outcome has been compared with the results of a CIS calculation, which does not suffer from the SI error and therefore gives the correct ordering of the excited states in the framework of the single-reference methods and does not underestimate the excitation energy of CT states.

Single-reference methods neglect doubly or higher excited configurations of the wave function, which are needed for a correct description of electron correlation energy. It is known that for conjugated systems like pyrene, the influence of doubly excited configurations is significant. To clarify the influence of the higher excited configurations, we used a variant of configuration interaction singles doubles (CISD) named 'scaled opposite spin CIS(D)′ (SOS-CIS(D)) methods[100] as implemented in Q-Chem.

Experimental results

Steady-state characterization

Absorption and fluorescence spectra (Fig. 2) were taken for the pyrene-modified adenosine (PyA, Fig. 1) in eight different solvents, subdivided into two classes, protic (MeOH, EtOH, iPrOH and *t*BuOH) and aprotic (DMSO, DMF, acetone and EtOAc) solvents. The solvents of each class were chosen to cover a broad permittivity range (Table 1).

Absorption. Absorption spectra of PyA show a structured absorption band in the range from 325 nm to 420 nm for each solvent with two main maxima and several minor absorption shoulders (Table 1 and Fig. 2). The low energetic absorption

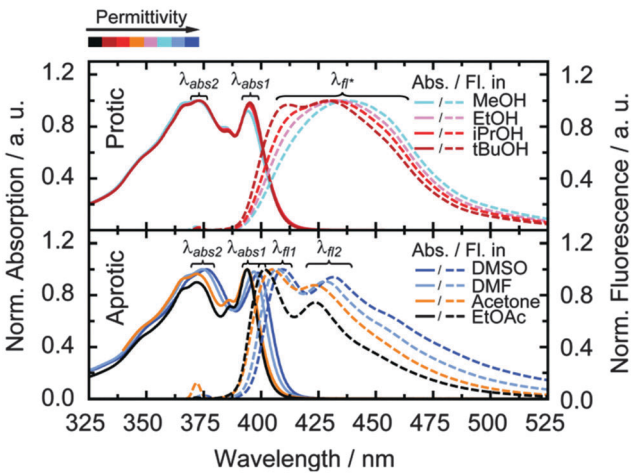

Fig. 2 Normalized absorption (solid lines) and normalized fluorescence (dashed lines) spectra for pyrene modified adenosine (150 μM and 10 μM, respectively) in four protic (upper panel) and four aprotic (lower panel) solvents. For the fluorescence spectra PyA was excited at λ_{abs2}: MeOH – 372 nm, EtOH, iPrOH and *t*BuOH – 373 nm, DMSO – 376 nm, DMF – 374 nm, Acetone and EtOAc – 372 nm.

Table 1 PyA steady-state spectral characteristics measured in different solvents. ε_r: permittivity of pure solvent without the 1% DMSO fraction.[101] λ_{abs2} and λ_{abs1}: main absorption peaks. λ_{fl1} and λ_{fl2}: main fluorescence peaks. * estimated by center of mass at half amplitude. Φ_{fl}: fluorescence quantum yield

PyA in		ε_r[101]	Abs./nm		Fluor./nm		Φ_{fl}
			λ_{abs2}	λ_{abs1}	λ_{fl1}	λ_{fl2}	
Aprotic	DMSO	47.2	376	399	410	432	0.79
	DMF	38.3	374	397	407	428	0.76
	Acetone	21.0	371	394	405	424	0.84
	EtOAc	6.1	371	394	399	422	0.78
Protic	MeOH	33.0	371	394	440*		0.79
	EtOH	25.3	372	395	437*		0.79
	iPrOH	20.2	372	395	434*		0.76
	*t*BuOH	12.5	372	395	431*		0.72

maximum (λ_{abs1}) is located at approx. 396 nm, while the energetically higher one (λ_{abs2}) is around 374 nm. Above 400 nm, the absorption steeply drops. No dimerization of PyA could be observed up to a concentration of 2 mM. In protic solvents, the ratio of the main absorption peaks changes slightly in favour of the second absorption peak. The second absorption maximum (λ_{abs2}) shows no significant change in the spectral position. For aprotic solvents, we observe with increasing solvent permittivity from EtOAc to DMSO a bathochromic shift of 5 nm. Additionally, a slight amplitude ratio change occurs in favour of the second absorption maximum.

Emission. Emission spectra of PyA were taken for each solvent by exciting the absorption band around 374 nm (Table 1, λ_{abs2}). No changes in spectral behavior were observed for other excitation wavelengths between 350 nm and 450 nm. In all solvents, PyA shows intense fluorescence between 390 nm and 600 nm. The spectral properties strongly depend on the solvent type and the permittivity (Fig. 2). Increasing permittivity leads to a bathochromic shift of the fluorescence maxima for both solvent classes (Table 1).

In protic solvents, the fluorescence is in general broad and unstructured with weak shoulders, which get more pronounced with decreasing permittivity. Accordingly, the fluorescence splits into two clearly distinguishable maxima at 412 nm and 426 nm in *t*BuOH.

In aprotic solvents, a fine structure is visible in the fluorescence spectra, which undergoes a bathochromic shift by ~10 nm with increasing permittivity.

Fluorescence quantum yields are around 0.8 for both solvent classes (Table 1, Φ_{fl}). In aprotic solvents, the fluorescence quantum yield shows no clear tendency with respect to the solvent permittivity, whereas protic solvents cause a slight increase of the fluorescence quantum yield with increasing permittivity.

Transient absorption of PyA in MeOH

TA measurements were performed to further elucidate the solvent and permittivity dependence of PyA in all eight solvents. They revealed a complex time-dependent behaviour with the same number of components, which differ only in their amplitude and temporal progression in each solvent. Therefore, we will point out our course of analysis exemplary for the methanol dissolved sample. The spectral characteristics and lifetimes in the other solvents are described thereafter and are summarized in Table 2.

In MeOH, the TA spectrum (Fig. 3B) shows three different main signals that cannot be separated clearly. The ground-state bleach (GSB, negative amplitude) is visible from 371 nm to ~410 nm. The GSB signal partially overlaps with a structured stimulated emission (SE, negative amplitude), which dominates the spectrum between 400 nm and 500 nm. At longer wavelengths (>500 nm), broad and structured excited-state absorption (ESA, positive amplitude) is present, which extends beyond the spectral window of the measurements (~690 nm).

ESA characteristics. The steady state fluorescence and absorption spectra (Fig. 3B, upper panel) indicate no relevant contributions of SE and GSB are in the ESA spectral region above 550 nm. Thus, all spectral characteristics and dynamics above 550 nm solely belong to the excited state absorption. The maximum at 663 nm (λ_{ESA1}) and the two shoulders at 623 nm and 639 nm (Fig. 3A, lower panel) can be assigned to

Table 2 Time resolved properties of PyA in different solvents. λ_i (i = ESA1/2 and SE1/2): wavelengths or wavelength ranges of the respective bands observed in the TA. λ_{ESA2} and λ_{SE2} were selected by the isosbestic points between SE1, SE2, ESA2 and ESA1 within the first 10 ps. λ_{ESA2S}: spectral position of the ESA2 maximum at 1500 ps. λ_{trfl1}: fluorescence intensity maxima at time zero (SC measurements), λ_{trfl2}: after the spectral shift (SC measurements). τ_1 (IVR), τ_2 (S_{1x} population) and τ_3 (solvent dependent stabilization of S_{1x}) estimated through LDM. τ_4 overall liftetime of PyA fluorescence measured with the streak camera.* τ_4 was not exactly determinable by TA measurements, but is larger than 1 ns

PyA in		Time resolved data							Lifetimes			
		Transient absorption (TA)					Streak camera (SC)					
		Excited state abs./nm			Stimulated emission/nm		Fluorescence/nm		TA/ps			SC/ns
		λ_{ESA1}	λ_{ESA2}	λ_{ESA2S}	λ_{SE1}	λ_{SE2}	λ_{trfl1}	λ_{trfl2}	τ_1	τ_2	τ_3	τ_4*
Aprotic	DMSO	666	575–n.d.		403	450–575	410	432	0.2	3.7		2.1
	DMF	661	545–n.d.		401	430–545	n.d.	n.d.	0.3	3.7		n.d.
	Acetone	664	515–660		398	420–515	n.d.	n.d.	0.3	3.7		n.d.
	EtOAc	662	515–670		398	420–515	399	422	0.2	3.7		1.8
Protic	MeOH	663	515–630	608	399	435–515	432	440	0.3	2–10	10–20	2.4
	EtOH	663	515–650	611	399	425–515	n.d.	n.d.	0.2	9.6	76	n.d.
	iPrOH	663	520–655	613	398	420–520	n.d.	n.d.	0.2	17	130	n.d.
	*t*BuOH	662	520–655	614	398	420–520	427	430	0.2	11	170	1.8

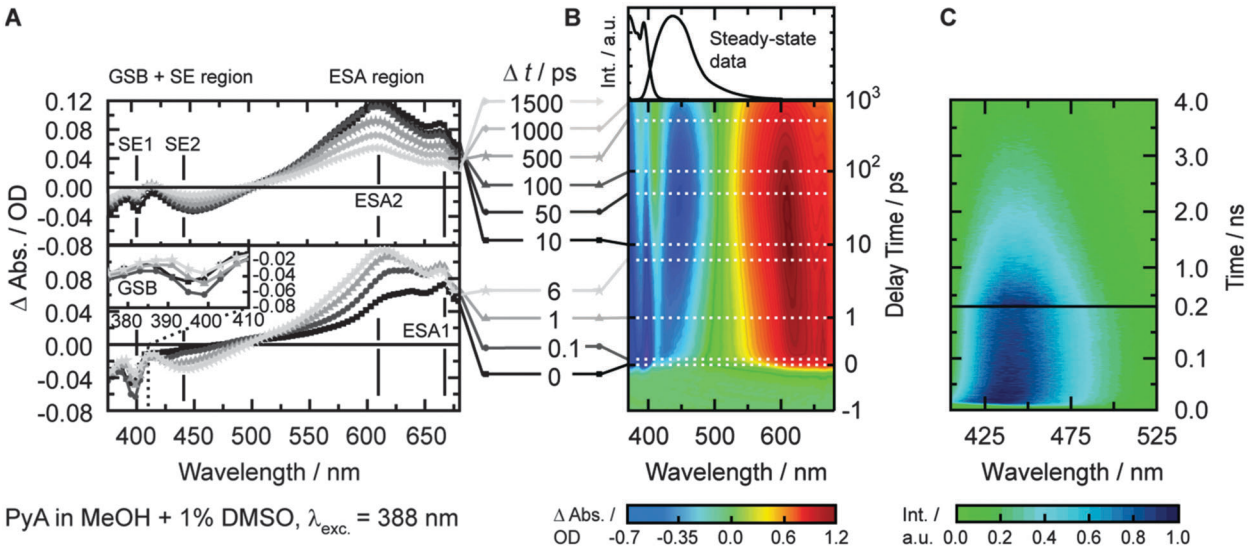

Fig. 3 Dataset for PyA in MeOH and 1% DMSO excited at 388 nm. (A) Time slices between 0 ps and 6 ps (lower panel) as well as 10 ps and 1500 ps (upper panel). Inset shows GSB with superimposed SE. (B) Contour plot between −1 ps and 1000 ps, with highlighted positions of time slices (dashed lines). (C) Streak camera measurements with a ~5 ns decay window (upper panel) and a ~0.5 ns decay window (lower panel).

one ESA band (ESA1), which arises during the first 500 fs. Subsequently, an unstructured excited state absorption (ESA2) arises within 6 ps with a maximum intensity around 614 nm (λ_{ESA2}), while the ESA1 band slightly loses amplitude. The ESA2 band then shifts spectrally towards 608 nm (λ_{ESA2S}) (Fig. 3A, upper panel). By plotting the spectral position of the ESA2 maximum against the delay time after excitation, two time constants (λ_{ESA2^a} = 1.8 ± 0.3 ps, λ_{ESA2^b} = 22 ± 3 ps) were found for the hypsochromic spectral shift (Fig. 4B, red curve). The short one (λ_{ESA2^a}) is related to the appearance of the ESA2 and the long one (λ_{ESA2^b}) describes the spectral shift of the ESA2. Finally, both ESA bands decay with time constants beyond the experimental accessible time range of 1.5 ns.

GSB and SE characteristics. The GSB minima at 395 nm (λ_{abs1}) and at 375 nm (λ_{abs2}) (Fig. 3A, lower panel) correspond to the positions of the steady state absorption maxima. The signal at 375 nm reflects primarily the GSB dynamics while the minimum at 395 nm is superimposed by SE (Fig. 3A). Thus, the amplitude at 395 nm is at early times higher than anticipated by the steady-state absorption spectra. Around 400 nm (λ_{SE1}) a spectral shift of the SE is observable during the first few 100 fs (Fig. 3A, inset lower panel), resulting in a structured SE band (SE1). Within 6 ps, another stimulated emission band (SE2) arises between 435 nm and 515 nm with a maximal amplitude at ~443 nm, while the SE1 loses amplitude (Fig. 3A, lower panel). This second stimulated emission band subsequently shifts bathochromically (SE2S) into the ESA region. Due to this, the expected amplitude ratio of the GSB minima, based on the steady-state absorption spectra, is observed.

ESA in the SE region. Because of the spectral overlap of ESA and SE, strong compensation of the different contributions in the spectral region around 500 nm occurs.

Since the SE signal is negative in TA, the slightly positive signal after 50 ps at 411 nm (Fig. 3A) means that we observe a broad ESA1 band. A broad ESA in this region is typical for pyrene and its derivatives.[6,8,16,19,23,56] This ESA, which is superimposed by the SE, prevents a proper quantification of the spectral shift and the determination of the exact spectral position of the SE2 band.

Streak camera measurements

Streak camera measurements were performed to obtain the fluorescence dynamics without the disturbing contributions of ESA and GSB (Fig. 3C). DMSO, EtOAc, MeOH and *t*BuOH were chosen as representative solvents with the largest change in permittivity for each solvent class.

The time frame of ~0.5 ns revealed a transient spectral shift of ~8 nm (~420 cm^{-1}) from 432 nm to 440 nm with a time constant of 17 ± 1 ps (Fig. 4B, τ_{SE2^b}, blue curve). The spectral shift occurs with a similar time constant like the slow component of the ESA2 shift (τ_{ESA2^b} = 22 ps), so these two time constants should describe the same process. The lack of the fast time constant obtained for the ESA2 shift (τ_{ESA2^a} = 1.8 ps) can be explained by the limited time resolution of the streak camera.

Streak camera measurements with a time frame of ~5 ns revealed an overall lifetime (τ_4) of 2.0 ± 0.1 ns (Fig. 3C, upper plot).

Summary of the time-resolved behaviour

After photo-excitation, the appearance of structured bands ESA1 and SE1 during the first 500 fs is observed. Within less than 6 ps, ESA1 and SE1 slightly lose amplitude. At the same time, the unstructured ESA2 and SE2 bands gain amplitude. The ESA1 band is correlated with the SE1 band and the ESA2 band with the SE2 band, respectively. Both ESA bands and SE bands are energetically close. ESA2 and SE2 spectrally shift towards each other within 10–20 ps. The spectral shift is also visible in the time-resolved fluorescence measurements and could be analysed in detail only in MeOH, because of the

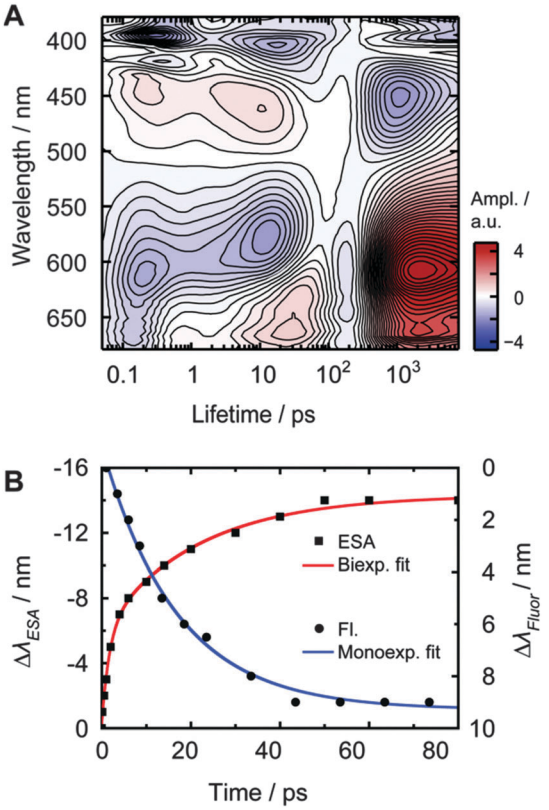

Fig. 4 Analysis of PyA in MeOH and 1% DMSO excited at 388 nm. (A) Lifetime density amplitude map. (B) Spectral shift of the unstructured ESA2 maximum (cubes) and biexponential fit (red line, τ_{ESA2a} = 1.8 ± 0.3 ps and τ_{ESA2b} = 22 ± 3 ps), as well as spectral shift of the fluorescence maximum (circles) measured with the streak camera and monoexponential fit (blue line, τ_{SE2b} = 17 ± 1 ps).

spectroscopically hardly separable emitting states. All signals decay with a lifetime of approximately 2 ns, as determined by the streak camera measurements.

LDM of PyA in MeOH

In methanol, the LDM for PyA (Fig. 4A) shows a first time constant (τ_1) around 200 to 300 fs, which is within our time resolution. Minima at 395 nm, 419 nm, 611 nm and 662 nm and a maximum at 445 nm are observable. These extremes represent a change in amplitude due to IVR, observable in the SE1 and ESA1 bands.

Between ~2 ps and ~30 ps, elongated extremes at 445 nm and 611 nm are visible. The maximal intensity of these extremes shifts towards each other with increasing lifetime. They are composed of two separate lifetimes, which are hardly distinguishable in MeOH. This conclusion is supported by the LDM of PyA in other solvents, where the separation is clearly visible (Fig. 5). Furthermore, the fit of the spectral ESA shift (Fig. 4B) also shows two lifetimes. The shorter of these two lifetimes (τ_2, ~2–10 ps) describes the increase of the ESA2. The longer one (τ_3, ~10–20 ps) dominates the signals and describes the spectral shift. The signals around 20 ps at 404 nm and 663 nm are a consequence of the spectral shift (Fig. 4).

Lifetimes between 1 ns and 3 ns show a broad distribution at 452 nm, 606 nm and 626 nm, which describe the decay of both, SE and ESA bands. The longest lifetimes cannot be completely recovered from the LDMs, due to the limited amount of data points and limited time range. Therefore, the overall decay lifetime τ_4 was determined by fluorescence measurements (Table 2).

Comparison of the spectral behavior of PyA in different solvents

After the fast spectral shift of the ESA1 band (Fig. 5 and Table 2, τ_1 = 0.2–0.3 ps), strong solvent class and permittivity

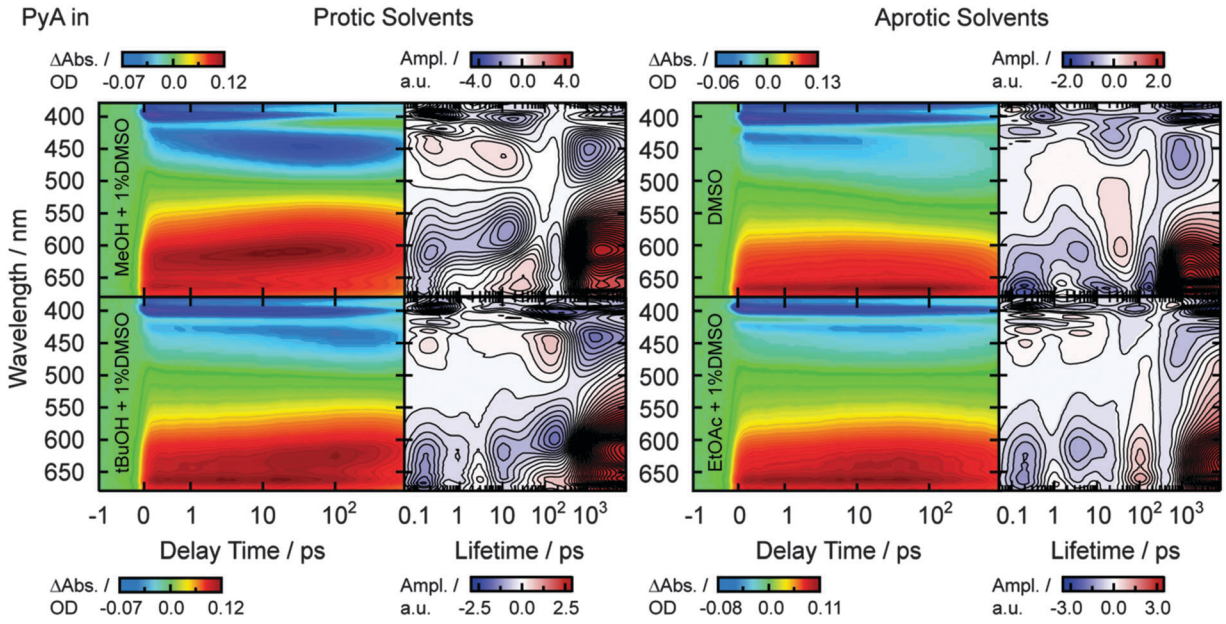

Fig. 5 Transient absorption spectra (λ_{exc} = 388 nm) and LDM of PyA in protic solvents (MeOH and *t*BuOH, left side) and in aprotic solvents (DMSO and EtOAc, right side). MeOH and DMSO as the upper limit of the measured permittivity range of each solvent class and *t*BuOH and EtOAc as the lower limit.

dependencies are visible. The spectral position of ESA1 changes slightly to longer wavelengths with increasing permittivity in aprotic solvents (Table 2, λ_{ESA1}). This is also the case for the ground state absorption (Fig. 2 and Table 1, λ_{abs1}).

In protic solvents, strong mostly unstructured ESA2 and SE2 bands appear within 20 ps (Table 2, τ_2). A higher solvent permittivity leads to slightly larger amplitudes of ESA2 and SE2 bands. Additionally, the following hypsochromic shift of ESA2 and bathochromic shift of SE2 is stronger and becomes linearly faster with increasing permittivity (Table 2, τ_3).

In aprotic solvents, a weak unstructured ESA2 (SE2) band appears with a time constant of $\sim$3.7 ps, which is slightly faster than in protic solvents (Table 2, τ_2). In DMSO and DMF, the ESA2 band is largely superimposed by the ESA1 band, while spectrally separated in EtOAc and acetone. Like in protic solvents, the ESA2 (SE2) amplitude increases with increasing permittivity, but is in general low when compared to protic solvents (Fig. 5). A spectral shift of the SE2 band is observable only in DMSO and DMF, but not visible in their ESA2 bands. This can be explained by the spectrally close and strong ESA1 band, which is superimposed on the much weaker ESA2 in aprotic solvents. However, a spectral shift of the SE2 is assumed for all solvents due to the spectral shift observed in the steady-state emission spectra.

The overall lifetime was determined *via* streak camera measurements for representatives of both solvent classes with the highest and lowest permittivity. In both solvent classes, τ_4 is in the range of 2 ns and increases with the solvent permittivity (Table 2, $\Delta\tau_4^{protic} \approx 0.6$ ns, $\Delta\tau_4^{aprotic} \approx 0.3$ ns).

Results of quantum chemical calculations of PyA

Ground state geometry optimization

For this study the PyA molecule has been fully optimized in the electronic ground-state using DFT with the above mentioned xc-functionals (B-LYP, B3-LYP and BH-LYP) and Dunnnings double zeta basis set (DZP) as implemented in Turbomole. Calculations were done in vacuum neglecting solvent interactions.

Optimized ground state structures show a planar arrangement of the base and the pyrene moiety independent of the applied method. The ribose is coordinated to the adenosine by an intramolecular H-bond between the 2′ OH of the ribose and the N3 atom of the base (Fig. 6).

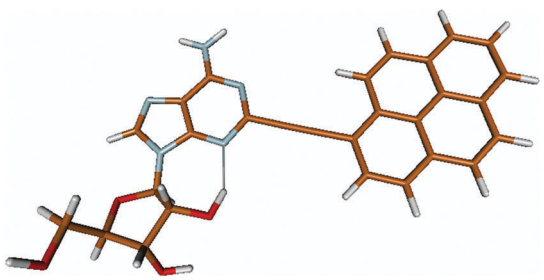

Fig. 6 Ground state optimized structure of PyA (DFT/BH-LYP).

Method evaluation

The vertically excited states have been calculated from the ground state optimized structures using the corresponding methods (Table 3) and the DZP basis set. For the SOS-CIS(D) method the BH-LYP optimized structure has been used along with the DZP basis set and the SVP auxiliary fitting basis set.

As one can see from Table 3, for the TDDFT methods the excited states show a functional dependent blue shift of the excitation wavelengths of the transitions (E_{exc}). This is due to the admixture of increasing amounts of HF-exchange (B-LYP < B3-LYP < BH LYP) in the different functionals.

xc-functional study and influence of the SI error. The ordering of the excited states of PyA is highly functional dependent (Table 3) due to the influence of the SI error. The comparison with the CIS method shows that the B-LYP functional fails completely to predict the right ordering of states and many spurious CT states are found in the calculated spectrum.

Table 3 Vertical transitions from ground state to excited states and the corresponding orbital characters. E_{exc} is the excitation wavelength. f_{OSC} is the calculated oscillator strength for the transition from the ground state to the corresponding excited state

Transition: $S_0 \rightarrow$	E_{exc}/nm	Character			f_{OSC}
		B-LYP			
S_1	475.3	HOMO	−LUMO	(78%)	0.67
S_2	447.0	HOMO − 1	−LUMO	(62%)	0.108
S_3	426.3	HOMO − 2	−LUMO	(96%)	0.0011
		B3-LYP			
S_1	403.5	HOMO	−LUMO	(95%)	0.95
S_2	355.1	HOMO − 1	−LUMO	(40%)	0.011
		HOMO	−LUMO + 1	(28%)	
		HOMO − 2	−LUMO	(20%)	
S_3	335.5	HOMO − 1	−LUMO	(42%)	0.0064
		HOMO − 2	−LUMO + 1	(35%)	
		HOMO	−LUMO + 1	(18%)	
		BH-LYP			
S_1	348.2	HOMO	−LUMO	(92%)	1.043
S_2	309.0	HOMO − 2	−LUMO	(28%)	0.006
		HOMO	−LUMO + 1	(25%)	
		HOMO − 1	−LUMO	(21%)	
S_3	270.1	HOMO − 1	−LUMO	(46%)	0.421
		HOMO	−LUMO + 2	(26%)	
		CIS			
S_1	334.5	HOMO	−LUMO	(79%)	0.92
S_2	288.3	HOMO − 1	−LUMO	(34%)	0.0017
		HOMO	−LUMO + 1	(26%)	
		HOMO − 2	−LUMO	(12%)	
S_3	254.0	HOMO	−LUMO + 2	(22%)	0.438
		HOMO − 1	−LUMO	(14%)	
		SOS-CIS(D)			
S_1	330.9	HOMO − 1	−LUMO	(40%)	0.0045
		HOMO	−LUMO + 1	(18%)	
S_2	287.5	HOMO	−LUMO	(79%)	1.3
S_3	226.5	HOMO	−LUMO + 2	(26%)	0.58
		HOMO − 1	−LUMO	(13%)	

B3-LYP performs better than the B-LYP functional, but still the ordering of states differs from the CIS results. For example the third excited state (S_3) can be identified as an intruder state, which has been calculated at much too low energy compared to the CIS method. This is a result of its high CT character and the SI error of TDDFT.

The increased amount of HF exchange in the BH-LYP functional corrects for this error and so the state ordering is in agreement with the CIS results.

Influence of double excitations. The picture changes dramatically looking at the SOS-CIS(D) results (Table 3). The double-excitation method stabilizes the dark PyA S_2 state by almost 1 eV, but still only one bright and one dark state are observed, while the transition to the bright state remains a HOMO to LUMO transition. The influence is much lower for the bright S_1 and S_3 states. They get slightly destabilized by 0.06 eV and 0.03 eV, respectively. As a result, the ordering of the states is reversed, compared to the results of the single reference methods discussed above. Hence, the dark state of PyA now becomes the lowest excited state. The SOS-CIS(D) method predicts the ordering of the first two excited states of PyA to be the same as for the unsubstituted pyrene. This finding is not in agreement with the experimental excitation spectra of PyA (see ESI†). There are no signs of a low lying dark state in the excitation spectra (Fig. S2, ESI†) and only a weak Stokes shift is observable. The SOS-CIS(D) method probably over-stabilizes the dark state, but it shows that the impact of the double excitation method is large for this state. Unfortunately, it is not feasible to treat big systems like PyA with quantum mechanical methods that explicitly include higher excitations (like *e.g.* CISDT, which accounts for singly, doubly and triply excited configurations) to verify the exact energetics of the optically forbidden state. However, the exact energy of the dark state is not critical for the further discussion of the excited state dynamics. For the following discussion we refer to the BH-LYP results, which are in good agreement with our experimental data.

Comparison with experimental data

All DFT calculations and the CIS method show an optically allowed $S_0 \rightarrow S_1$ transition with a high oscillator strength of 0.7–1 (Table 3), which corresponds to a HOMO–LUMO transition.

The second excited state (S_2) is a dark state. For the BH-LYP method, the $S_0 \rightarrow S_2$ transition has a complex character and possesses three dominant contributions, namely a HOMO − 1 to LUMO, a HOMO to LUMO + 1 and a HOMO − 2 to LUMO transition.

The optically allowed transition to the third excited state (S_3) corresponds to a HOMO − 1 to LUMO and a HOMO to LUMO + 2 transition.

It should be noted that the energy difference between the two allowed transitions ($S_0 \rightarrow S_1$ and $S_0 \rightarrow S_3$) calculated with the BH-LYP and CIS methods is in reasonable agreement with the experimental data. A comparison between the calculated and measured absorption spectra can be found in the ESI† (Fig. S4).

Comparison between PyA and pyrene. In the case of pyrene,[102] the $S_0 \rightarrow S_1$ transition has practically zero oscillator strength and corresponds to a mixture of a HOMO − 1 to LUMO and a HOMO to LUMO + 1 transition with equal contributions. The $S_0 \rightarrow S_2$ has high oscillator strength and is described by a HOMO to LUMO transition.

In contrast to this the PyA $S_0 \rightarrow S_1$ transition has high oscillator strength (Table 3) and corresponds to a HOMO to LUMO transition. Comparing the molecular orbitals (MOs) of PyA with the ones of pyrene (Table 4) this transition is similar to the bright $S_0 \rightarrow S_2$ transition of pyrene. The contributing molecular orbitals for the transition to the S_1 state in PyA and S_2 state in pyrene are only slightly influenced by substitution on the pyrene 1 position, Table 4.

The second excited state (S_2) of PyA is a dark state like the S_1 state of pyrene. The $S_0 \rightarrow S_2$ transition has a complex character like the $S_0 \rightarrow S_1$ transition of pyrene, but possesses an additional third dominant contribution, namely a HOMO − 2 to LUMO transition. The PyA HOMO − 2 is similar to the pyrene HOMO − 1 orbital, but the PyA HOMO − 1 orbital is not comparable to any of the pyrene orbitals. The additional transition shows the strong influence of the substitution on the transition character. Thus in the case of PyA, the original pyrene S_1 state gets destabilized and becomes the PyA S_2 state.

Summing up these findings, we can conclude that within the framework of the single reference methods the ordering of the

Table 4 Molecular orbitals of PyA and pyrene (DFT/BH-LYP orbitals displayed, the orbitals are independent of the chosen method). Note: Pyrene HOMO − 1 orbital corresponds to the PyA HOMO − 2 orbital

	PyA	Pyrene
LUMO + 1	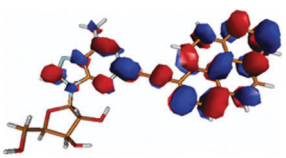	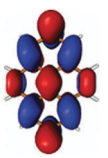
LUMO	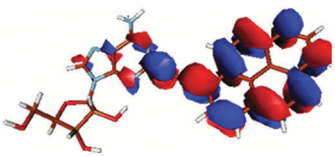	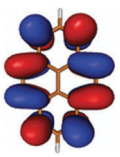
HOMO	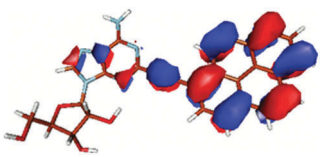	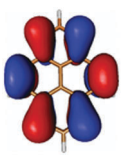
HOMO − 1	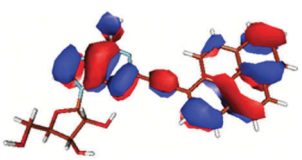	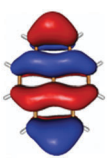
HOMO − 2	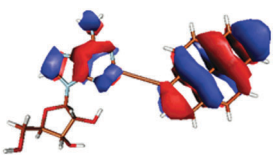	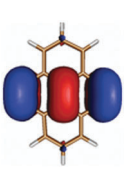

excited states of PyA is reversed with respect to the excited states of pyrene. Accordingly, the fluorescent state of PyA is the S_1 state which explains the observed small Stokes shift of the PyA fluorescence, compared to the large Stokes shift for pyrene.

Discussion

The model of the photophysics shown in Fig. 7 summarizes, extends and adjusts the originally proposed one[61] with new insights into the nature of the states and the photo-dynamics.

Ground state properties

In general, the substitution pattern of pyrene strongly influences the spectral position as well as the oscillator strength for $S_0 \rightarrow S_1$ and $S_0 \rightarrow S_2$ transitions in absorption and fluorescence spectra depending on the position[11,15,103] and the electrochemical nature of the substituent.[103,104] Especially, the 1-position of pyrene (Fig. 1) shows strong electronic coupling with its substituents.[11,15,23] Therefore, the absorption spectrum of PyA strongly differs from that of pyrene.

Quantum chemical calculations revealed one optically allowed and one forbidden transition in the spectral range between 325 nm to 420 nm, but were not able to describe a clear order of the states. In the case of pyrene, fluorescence (according to Kasha's rule) occurs from the S_1 state, which has very low oscillator strength. Therefore, pyrene fluorescence shows a pronounced Stokes shift ($\sim$40 nm) and is long-lived ($\sim$238 ns in DMSO).[3] PyA shows a weak Stokes shift ($\sim$10 nm in DMSO, Table 2) of the emission and is short-lived (τ_4, $\sim$2 ns). In addition with the structural similarity to the pyrene emission, this indicates that we observe a $S_0 \rightarrow S_1$ transition. The high fluorescence quantum yield ($\sim$0.8) implies that this transition has high oscillator strength. This rules out excitation into higher energetic states at 388 nm. Therefore, the fine structure of the absorption band between 325 nm and 420 nm (Fig. 2) is the result of a superimposed vibrational fine structure like in the case of unsubstituted pyrene.

A change of the absorption ratio from the first (λ_{abs1}) towards the second (λ_{abs2}) maximum, which is accompanied by a bathochromic shift, is observed in aprotic solvents with increasing permittivity. No spectral shift and a much weaker change of the absorption ratio is observed in protic solvents, this indicates a intermolecular hydrogen-bond based alteration of the ground-state electron-density distribution, which reduces the influence of the permittivity on PyA. In aprotic solvents, the changes in the absorption spectra are a result of the changing solvent permittivity, which is due to the lack of solvent hydrogen bonding. In particular, the hydrogen bond between N3 and the 2′OH group observed in the quantum chemical calculations should influence the photo-dynamics.

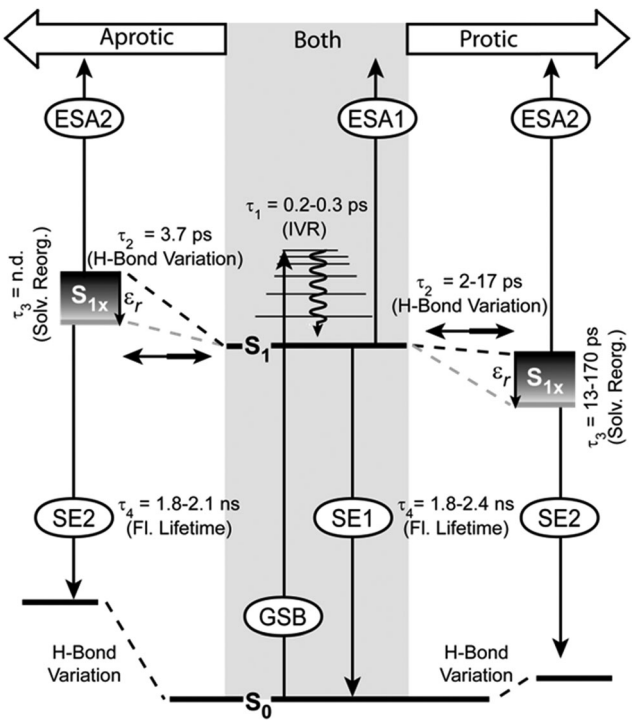

Fig. 7 Model of relaxation pathways and observed signals in the TA for PyA in aprotic (left side) and protic (right side) solvents.

Excited state dynamics

In agreement with our previous findings,[61] two excited states and four time constants describe the photo-physics of PyA in MeOH sufficiently. The values of τ_1, τ_2 and τ_4 remain in the same time range. The time constant τ_3 (10–20 ps), which describes the spectral shift, differs by one order of magnitude (τ_3 = 470 ps).[60] This difference in the new datasets is a result of the higher spectral resolution and the improved analysis approach. By using lifetime density maps, the shortcoming of an exponential global fit analysis for spectral shifts, which are influenced linearly by time, was overcome.

Development of S_1 substates

The S_1 state is spectrally represented by the ESA1 and SE1 signals. Between 325 nm to 420 nm higher vibronic S_1 states are excited, therefore the first time constant (τ_1) can be attributed to intramolecular vibrational energy redistribution (IVR). The IVR is not influenced by the varying solvents and lies around 0.2 ps to 0.3 ps in all solvents, which is a typical value for pyrene.[6,8,12] The spectral positions of the ESA1 and the ground state absorption bands shift weakly ($\sim$10 nm) to longer wavelengths with increasing solvent permittivity. This indicates that the S_0 and the S_1 state differ only slightly in their dipole moment. This explains why the S_1 state and therefore the ESA1 and the SE1 bands do not show significant solvent dependencies. The molecule in the S_1 state can partially adopt another conformation within τ_2, which belongs to the same potential energy surface. The conformation of this substate is unknown, but energetically close to the initial conformation. This conformational substate is further on called the S_{1x} state. The S_{1x} state manifests itself in the TA by the ESA2 and the SE2 bands.

In aprotic solvents, the ESA1 signal is dominant and therefore the S_1 state is mostly populated. Streak camera and steady-state spectra are dominated by a structured emission in

aprotic solvents, showing that the S_1 state is the origin of the structured emission.

In protic solvents, both bands possess high amplitudes and therefore a significantly populated S_{1x} state can be assumed. A high S_{1x} state population is accompanied by an unstructured red-shifted emission (Fig. 2).

Emission wavelengths which represent either mostly the S_1 state (410 nm) or the S_{1x} state (450 nm) do not differ in their excitation spectra (Fig. S2, ESI†). This finding supports the model that the relaxed S_1 state populates the S_{1x} state (Fig. 7).

S_{1x} state properties

Either the S_1 state or the S_{1x} state emission dominate the spectra, while no significant differences in the fluorescence quantum yields are noticeable in the different solvent classes. This implies that S_1 and S_{1x} exhibit similar fluorescence quantum yields. This rules out a strong intramolecular charge transfer character of the S_{1x} state, because this would result in a strong reduction of the fluorescence quantum yield and a much stronger bathochromic shift of the emission maximum with increasing solvent permittivity.[14,22,105,106] Then again, a small transfer of electron density, which is not localized on a functional group, does not strongly alter the fluorescence properties.[106] The HOMO and LUMO ($S_0 \rightarrow S_1$) show partial electron density contributions on the nucleobase. A weak delocalized CT character of the S_{1x} state also explains the spectral shift of the SE2 band (τ_3). This bathochromic shift reflects a solvent-permittivity dependent stabilization of the S_{1x} state due to solvent reorganization. Higher solvent permittivity leads to a stronger spectral shift of the S_{1x} state (Fig. 5). The acceleration of the spectral shift with increasing solvent permittivity (Table 2, τ_3) is a result of faster solvent reorganization, due to the stronger electrostatic interactions between PyA and the solvents with a high permittivity.

Thus, a slight electron density transfer, which leads to a slightly more polar S_{1x} state, is sufficient to explain the experimental findings. The reaction coordinate, which describes the transition to the S_{1x} state, could not be determined by quantum chemical calculations due to the size of the system.

Solvent dependence of equilibrium population

As mentioned above, a high solvent permittivity and protic solvents, which are able to form hydrogen bonds, lead to a higher S_{1x} population. This is visible in the reduced share of structured emission. The exact population ratio between the S_1 state and the S_{1x} state is not quantifiable, due to the strong overlap of the SE with the ESA bands and because of the (most probably) different transition dipole-moments of the ESA1 and the ESA2 transitions. Nevertheless, the solvent class and the solvent permittivity allow the control of the population ratio. Increased S_{1x} population results from an energetic stabilization of the S_{1x} state (Fig. 7). The influence of the solvent class on the population ratio is much stronger than the permittivity. In aprotic solvents, the S_1 state is favoured even for solvents with high permittivity. In protic solvents, the situation is reversed and the S_{1x} state is more highly populated even in solvents with a low permittivity (Fig. 5). Therefore, the S_{1x} state has to be energetically more stable than the S_1 state (Fig. 7). Even though the energetic position of the S_{1x} state varies, the spectral position of the SE2 band is only weakly affected. This means that the ground state has to be equally affected in its energetic position.

Interestingly, only one decay time for S_1 and S_{1x} is observed in the streak camera measurements, which is in the same range for both solvent classes and varies only slightly with permittivity (Table 2, τ_4). In *t*BuOH for example, S_1 and S_{1x} are nearly equally populated, but do not show an additional decay lifetime in the streak camera measurements. This indicates, in combination with the energetic proximity of both states, that S_1 and S_{1x} undergo fast population exchange (τ_2), which leads to an equilibrium at the nanosecond timescale.

Hydrogen bond variation in the excited states

The intramolecular hydrogen bond between N3 and the 2'OH group in the ground state (S_0) restricts the glycosidic torsion and is also present in the S_1 state. The above mentioned solvent dependent behaviour leads us to the assumption that by reaching the S_{1x} state this bond is weakened by forming the conformation, which is connected to the S_{1x} state and influences the electron density on the adenine.

In the case of aprotic solvents (the S_{1x} state energetically higher than the S_1 state), the intramolecular hydrogen bond hinders the formation and makes this conformation unfavourable. The corresponding ground state is also destabilized with respect to the original S_0 state.

In protic solvents, the S_{1x} state is now energetically favoured relative to the S_1 state. This means that the surrounding solvent molecules probably form intermolecular hydrogen bonds with the N3 of adenine instead of the 2'OH group. The result is that the conformation of the S_{1x} state is now able to form and therefore energetically favoured.

Conclusions

Our systematic spectroscopic study provides detailed evidence that hydrogen bonding as well as the solvent permittivity strongly influence the photo-dynamics of PyA. Compared to a slightly different derivative of PyA[60] and PyA modified RNA,[61] the ultrafast dynamics vary in the excited state characteristics, assignments of time constants and provide new insights into the role of intramolecular hydrogen bonds (Fig. 7).

Higher vibronic states of the S_1 are excited between 325 nm to 420 nm and no contributions of other states are detectable. After IVR (τ_1), the locally excited S_1 state populates the conformational substate S_{1x} within τ_2. This S_{1x} state does not have a strong charge transfer character, but is slightly more polar than the S_1 state and hence gets stabilized by solvents with a high permittivity. The polar character of the S_{1x} state has to be the result of a restricted delocalized electron density distribution over the nucleobase. Due to that, τ_3 describes the solvent permittivity dependent stabilization of the S_{1x} state, rather than

the (previously assumed) decay of the S_1 state.[61] Therefore, the difference in magnitude of τ_3 to previous data is a result of the better resolved datasets and the improved analysis approach. Both emitting states (S_1 and S_{1x}) are in equilibrium and decay with the same time constant (τ_4).

However, the ground state and population ratio between the S_1 state and the S_{1x} state are strongly influenced by hydrogen bonds. A hydrogen bond between the 2'OH of the ribose and the N3 of the adenine for PyA was revealed by the quantum chemical calculations. This hydrogen bond influences the energetic position of the S_{1x} state depending on the solvent class. In aprotic solvents, the S_{1x} state is energetically destabilized relative to the S_1 state. This leads to the population ratio in favour of the S_1 state and therefore a structured fluorescence band. Protic solvents disturb this hydrogen bond by interfering *via* intermolecular hydrogen bonds. As a result, the S_{1x} state is energetically stabilized relative to the S_1 state and an unstructured fluorescence band is observed. In both solvent classes, a high permittivity further stabilizes the S_{1x} state independent of the S_0 state due to solvent reorganization, which results in a spectral shift and less structured fluorescence. No additional proton transfer could be observed.

These findings allow addressing even slight changes in the emission structure to permittivity changes in the surroundings of PyA upon *e.g.* ligand binding in RNA or to solvent inaccessible PyA positions.

Funding

The authors thank the Deutsche Forschungsgemeinschaft for funding *via* the Collaborative Research Center 902 'Molecular Principles of RNA-based Regulation'.

Acknowledgements

The authors thank Prof. Dr Wolfgang Zinth for the possibility to measure streak camera spectra. The authors would also like to thank Prof. Irene Burghardt and Prof. Andreas Dreuw for providing computational resources and financial support.

References

1 J. R. Lakowicz, *Principles of Fluorescence Spectroscopy*, Springer, New York, 3rd edn, 2010.
2 M. F. M. Post, J. Langelaar and J. D. W. van Voorst, *Chem. Phys. Lett.*, 1971, **10**, 468–472.
3 A. Nakajima, *Bull. Chem. Soc. Jpn.*, 1973, **46**, 2602–2604.
4 T. Kubota, K. Kano, B. Uno and T. Konse, *Bull. Chem. Soc. Jpn.*, 1987, **60**, 3865–3877.
5 P. Foggi, L. Pettini, I. Santa, R. Righini and S. Califano, *J. Phys. Chem.*, 1995, **99**, 7439–7445.
6 F. V. R. Neuwahl and P. Foggi, *Laser Chem.*, 1999, **19**, 375–379.
7 D. S. Karpovich and G. J. Blanchard, *J. Phys. Chem.*, 1995, **99**, 3951–3958.
8 M. Raytchev, E. Pandurski, I. Buchvarov, C. Modrakowski and T. Fiebig, *J. Phys. Chem. A*, 2003, **107**, 4592–4600.
9 T. Förster, *Angew. Chem.*, 1969, **81**, 364–374.
10 N. J. Turro, *Modern Molecular Photochemistry*, University Science Books, Sausalito, California, 1991.
11 A. G. Crawford, A. D. Dwyer, Z. Liu, A. Steffen, A. Beeby, L. O. Pålsson, D. J. Tozer and T. B. Marder, *J. Am. Chem. Soc.*, 2011, **133**, 13349–13362.
12 T. Fiebig, K. Stock, S. Lochbrunner and E. Riedle, *Chem. Phys. Lett.*, 2001, **345**, 81–88.
13 E. Pandurski and T. Fiebig, *Chem. Phys. Lett.*, 2002, **357**, 272–278.
14 J. Sung, P. Kim, Y. O. Lee, J. S. Kim and D. Kim, *J. Phys. Chem. Lett.*, 2011, **2**, 818–823.
15 C. Wanninger-Weiss and H.-A. Wagenknecht, *Eur. J. Org. Chem.*, 2008, 64–69.
16 C. E. Crespo-Hernandez, G. Burdzinski and R. Arce, *J. Phys. Chem. A*, 2008, **112**, 6313–6319.
17 Y. Niko, Y. Hiroshige, S. Kawauchi and G. Konishi, *Tetrahedron*, 2012, **68**, 6177–6185.
18 N. Amann, E. Pandurski, T. Fiebig and H.-A. Wagenknecht, *Angew. Chem., Int. Ed.*, 2002, **41**, 2978–2980.
19 N. Amann, E. Pandurski, T. Fiebig and H.-A. Wagenknecht, *Chem. – Eur. J.*, 2002, **8**, 4877–4883.
20 A. Trifonov, I. Buchvarov, H.-A. Wagenknecht and T. Fiebig, *Chem. Phys. Lett.*, 2005, **409**, 277–280.
21 A. Trifonov, M. Raytchev, I. Buchvarov, M. Rist, J. Barbaric, H.-A. Wagenknecht and T. Fiebig, *J. Phys. Chem. B*, 2005, **109**, 19490–19495.
22 C. Wagner and H.-A. Wagenknecht, *Chem. – Eur. J.*, 2005, **11**, 1871–1876.
23 P. Kaden, E. Mayer-Enthart, A. Trifonov, T. Fiebig and H.-A. Wagenknecht, *Angew. Chem., Int. Ed.*, 2005, **44**, 1637–1639.
24 C. Wanninger-Weiß, L. Valis and H.-A. Wagenknecht, *Bioorg. Med. Chem.*, 2008, **16**, 100–106.
25 A. Okamoto, K. Kanatani and I. Saito, *J. Am. Chem. Soc.*, 2004, **126**, 4820–4827.
26 K. Kawai, H. Yoshida, T. Takada, S. Tojo and T. Majima, *J. Phys. Chem. B*, 2004, **108**, 13547–13550.
27 Y. J. Seo, J. H. Ryu and B. H. Kim, *Org. Lett.*, 2005, **7**, 4931–4933.
28 Y. J. Seo, I. J. Lee, J. W. Yi and B. H. Kim, *Chem. Commun.*, 2007, 2817–2819.
29 M. Nakamura, Y. Fukunaga, K. Sasa, Y. Ohtoshi, K. Kanaori, H. Hayashi, H. Nakano and K. Yamana, *Nucleic Acids Res.*, 2005, **33**, 5887–5895.
30 H. Kashida, T. Takatsu, K. Sekiguchi and H. Asanuma, *Chem. – Eur. J.*, 2010, **16**, 2479–2486.
31 T. Kato, H. Kashida, H. Kishida, H. Yada, H. Okamoto and H. Asanuma, *J. Am. Chem. Soc.*, 2013, **135**, 741–750.
32 I. K. Astakhova, T. Santhosh Kumar, M. A. Campbell, A. V. Ustinov, V. A. Korshun and J. Wengel, *Chem. Commun.*, 2013, **49**, 511–513.
33 N. Venkatesan, Y. Jun Seo and B. Hyean Kim, *Chem. Soc. Rev.*, 2008, **37**, 648–663.

34 K. Huang and A. Martí, *Anal. Bioanal. Chem.*, 2012, **402**, 3091–3102.
35 R. Zhang, L. Yang, M. Zhao, J. Dong, H. Dong, Y. Wen, X. Zhan, H. Yang and G. Wang, *Polymer*, 2013, **54**, 1289–1294.
36 E. Mayer, L. Valis, C. Wagner, M. Rist, N. Amann and H.-A. Wagenknecht, *ChemBioChem*, 2004, **5**, 865–868.
37 G. T. Hwang, Y. J. Seo, S. J. Kim and B. H. Kim, *Tetrahedron Lett.*, 2004, **45**, 3543–3546.
38 G. T. Hwang, Y. J. Seo and B. H. Kim, *Tetrahedron Lett.*, 2005, **46**, 1475–1477.
39 L. Valis, E. Mayer-Enthart and H.-A. Wagenknecht, *Bioorg. Med. Chem.*, 2006, **16**, 3184–3187.
40 I. V. Astakhova, A. V. Ustinov, V. A. Korshun and J. Wengel, *Bioconjugate Chem.*, 2011, **22**, 533–539.
41 J. Huang, Y. Wu, Y. Chen, Z. Zhu, X. Yang, C. J. Yang, K. Wang and W. Tan, *Angew. Chem., Int. Ed.*, 2011, **50**, 401–404.
42 S. P. Sau and P. J. Hrdlicka, *J. Org. Chem.*, 2012, **77**, 5–16.
43 S. Srivatsan and A. Sawant, *Pure Appl. Chem.*, 2010, **83**, 213–232.
44 I. Tinoco Jr and C. Bustamante, *J. Mol. Biol.*, 1999, **293**, 271–281.
45 J. A. Cruz and E. Westhof, *Cell*, 2009, **136**, 604–609.
46 K. S. Karunatilaka and D. Rueda, *Chem. Phys. Lett.*, 2009, **476**, 1–10.
47 A. D. Garst, A. L. Edwards and R. T. Batey, *Cold Spring Harbor Perspect. Biol.*, 2010, 1–13.
48 A. Mahara, R. Iwase, T. Sakamoto, K. Yamana, T. Yamaoka and A. Murakami, *Angew. Chem., Int. Ed.*, 2002, **41**, 3648–3650.
49 A. Mahara, R. Iwase, T. Sakamoto, T. Yamaoka, K. Yamana and A. Murakami, *Bioorg. Med. Chem.*, 2003, **11**, 2783–2790.
50 O. A. Krasheninina, D. S. Novopashina and A. G. Venyaminova, *Russ. J. Bioorg. Chem.*, 2011, **37**, 244–248.
51 R. Waki, A. Yamayoshi, A. Kobori and A. Murakami, *Chem. Commun.*, 2011, **47**, 4204–4206.
52 K. K. Karlsen, A. Pasternak, T. B. Jensen and J. Wengel, *ChemBioChem*, 2012, **13**, 590–601.
53 T. Ueda, A. Kobori, A. Yamayoshi, H. Yoshida, M. Yamaguchi and A. Murakami, *Bioorg. Med. Chem.*, 2012, **20**, 6034–6039.
54 G. Wang, G. V. Bobkov, S. N. Mikhailov, G. Schepers, A. Van Aerschot, J. Rozenski, M. Van der Auweraer, P. Herdewijn and S. De Feyter, *ChemBioChem*, 2009, **10**, 1175–1185.
55 S. K. Silverman and T. R. Cech, *Biochemistry*, 1999, **38**, 14224–14237.
56 T. L. Netzel, K. Nafisi, J. Headrick and B. E. Eaton, *J. Phys. Chem.*, 1995, **99**, 17948–17955.
57 T. L. Netzel, M. Zhao, K. Nafisi, J. Headrick, M. S. Sigman and B. E. Eaton, *J. Am. Chem. Soc.*, 1995, **117**, 9119–9128.
58 A. Malakhov, E. Malakhova, S. Kuznitsova, I. Grechishnikova, I. Prokhorenko, M. Skorobogatyi, V. Korshun and Y. Berlin, *Russ. J. Bioorg. Chem.*, 2000, **26**, 34–44.
59 C. Grünewald, T. Kwon, N. Piton, U. Förster, J. Wachtveitl and J. W. Engels, *Bioorg. Med. Chem.*, 2008, **16**, 19–26.
60 U. Förster, N. Gildenhoff, C. Grünewald, J. W. Engels and J. Wachtveitl, *J. Lumin.*, 2009, **129**, 1454–1458.
61 U. Förster, C. Grünewald, J. W. Engels and J. Wachtveitl, *J. Phys. Chem. B*, 2010, **114**, 11638–11645.
62 U. Förster, K. Lommel, D. Sauter, C. Grünewald, J. W. Engels and J. Wachtveitl, *ChemBioChem*, 2010, **11**, 664–672.
63 S. Techert, S. Schmatz, A. Wiessner and H. Staerk, *J. Phys. Chem. A*, 2000, **104**, 5700–5710.
64 R. Huber, T. Fiebig and H.-A. Wagenknecht, *Chem. Commun.*, 2003, 1878–1879.
65 K. Suzuki, A. Kobayashi, S. Kaneko, K. Takehira, T. Yoshihara, H. Ishida, Y. Shiina, S. Oishi and S. Tobita, *Phys. Chem. Chem. Phys.*, 2009, **11**, 9850–9860.
66 A. M. Brouwer, *Pure Appl. Chem.*, 2011, **83**, 2213–2228.
67 L. Dworak, V. V. Matylitsky and J. Wachtveitl, *ChemPhysChem*, 2009, **10**, 384–391.
68 F. J. Lederer, F. F. Graupner, B. Maerz, M. Braun and W. Zinth, *Chem. Phys.*, 2014, **428**, 82–89.
69 G. Ryseck, T. Schmierer, K. Haiser, W. Schreier, W. Zinth and P. Gilch, *ChemPhysChem*, 2011, **12**, 1880–1888.
70 I. H. M. van Stokkum, D. S. Larsen and R. van Grondelle, *Biochim. Biophys. Acta, Bioenerg.*, 2004, **1657**, 82–104.
71 A. A. Istratov and O. F. Vyvenko, *Rev. Sci. Instrum.*, 1999, **70**, 1233–1257.
72 R. Croce, M. G. Müller, R. Bassi and A. R. Holzwarth, *Biophys. J.*, 2001, **80**, 901–915.
73 Z. Ablonczy, A. Lukács and E. Papp, *Biophys. Chem.*, 2003, **104**, 249–258.
74 V. A. Lórenz-Fonfría and H. Kandori, *Appl. Spectrosc.*, 2007, **61**, 74–84.
75 V. K. Mulligan, K. C. Hadley and A. Chakrabartty, *Anal. Biochem.*, 2012, **421**, 181–190.
76 V. A. Voelz and V. S. Pande, *Proteins: Struct., Funct., Bioinf.*, 2012, **80**, 342–351.
77 R.-J. Kutta, T. Langenbacher, U. Kensy and B. Dick, *Appl. Phys. B: Lasers Opt.*, 2013, **111**, 203–216.
78 E. T. Jaynes, *Phys. Rev.*, 1957, **106**, 620–630.
79 A. N. Tikhonov, *Dokl. Akad. Nauk SSSR*, 1963, **151**, 501–504.
80 K. Miller, *SIAM J. Math. Anal.*, 1970, **1**, 52–74.
81 P. Hansen, *BIT Numer. Math.*, 1990, **30**, 658–672.
82 J. Lian, D. Yao and B. He, in *Engineering in Medicine and Biology Society, 1998. Proceedings of the 20th Annual International Conference of the IEEE*, 1998, vol. 4, pp. 2155–2158.
83 J. Lian and B. He, *Brain Topogr.*, 2001, **13**, 209–217.
84 G. H. Golub, M. Heath and G. Wahba, *Technometrics*, 1979, **21**, 215–223.
85 V. A. Lórenz-Fonfría and H. Kandori, *Appl. Spectrosc.*, 2007, **61**, 428–443.
86 A. L. Dobryakov, S. A. Kovalenko, A. Weigel, J. L. Pérez-Lustres, J. Lange, A. Müller and N. P. Ernsting, *Rev. Sci. Instrum.*, 2010, **81**, 113106.
87 H. Satzger and W. Zinth, *Chem. Phys.*, 2003, **295**, 287–295.
88 R. Ahlrichs, *TurboMole V 5.10*, 2007.
89 J. Kong, C. White, A. Krylov, D. Sherrill, R. Adamson, T. Furlani, M. Lee, A. Lee, S. Gwaltney, T. Adams, C. Ochsenfeld,

A. Gilbert, G. Kedziora, V. Rassolov, D. Maurice, N. Nair, Y. Shao, N. Besley, P. Maslen, J. Dombroski, H. Daschel, W. Zhang, P. Korambath, J. Baker, E. Byrd, T. Van Voorhis, M. Oumi, S. Hirata, C. Hsu, N. Ishikawa, J. Florian, A. Warshel, B. Johnson, P. Gill, M. Head-Gordon and J. Pople, *J. Comput. Chem.*, 2000, **21**, 1532–1548.

90 E. Runge and E. K. U. Gross, *Phys. Rev. Lett.*, 1984, **52**, 997–1000.

91 M. E. Casida, *Recent Advances in Density Functional Methods, Part I*, World Scientific, Singapore, 1995.

92 J. E. D. Bene, R. Ditchfield and J. A. Pople, *J. Chem. Phys.*, 1971, **55**, 2236–2241.

93 A. Dreuw and M. Head-Gordon, *Chem. Rev.*, 2005, **105**, 4009–4037.

94 A. Dreuw, J. L. Weisman and M. Head-Gordon, *J. Chem. Phys.*, 2003, **119**, 2943–2946.

95 A. Dreuw and M. Head-Gordon, *J. Am. Chem. Soc.*, 2004, **126**, 4007–4016.

96 J. Plötner and A. Dreuw, *Chem. Phys.*, 2008, **347**, 472–482.

97 D. J. Tozer, *J. Chem. Phys.*, 2003, **119**, 12697–12699.

98 N. T. Maitra, *J. Chem. Phys.*, 2005, **122**, 234104.

99 J. Neugebauer, O. Gritsenko and E. J. Baerends, *J. Chem. Phys.*, 2006, **124**, 214102.

100 D. Casanova, Y. M. Rhee and M. Head-Gordon, *J. Chem. Phys.*, 2008, **128**, 164106.

101 D. R. Lide, *Handbook of Chemistry and Physics*, CRC Press, Boca Ranton, New York, London, Tokyo, 81st edn, 2000.

102 I. S. K. Kerkines, I. D. Petsalakis, G. Theodorakopoulos and W. Klopper, *J. Chem. Phys.*, 2009, **131**, 224315.

103 H. Maeda, T. Maeda, K. Mizuno, K. Fujimoto, H. Shimizu and M. Inouye, *Chem. – Eur. J.*, 2006, **12**, 824–831.

104 C. Yao, H.-B. Kraatz and R. P. Steer, *Photochem. Photobiol. Sci.*, 2005, **4**, 191–199.

105 Z. R. Grabowski, K. Rotkiewicz and W. Rettig, *Chem. Rev.*, 2003, **103**, 3899–4032.

106 A. Morimoto, T. Yatsuhashi, T. Shimada, L. Biczók, D. A. Tryk and H. Inoue, *J. Phys. Chem. A*, 2001, **105**, 10488–10496.

